MRI signal phase oscillates with neuronal activity in cerebral cortex: implications for neuronal current imaging

Jiaxin Du, Viktor Vegh*, and David C. Reutens

The University of Queensland, Centre for Advanced Imaging, Brisbane Queensland 4072, Australia

*To whom the correspondence should be addressed. E-mail: viktor.vegh@cai.uq.edu.au. Phone: +61-7-33460363

Abstract

Neuronal activity produces transient ionic currents that may be detectable using magnetic resonance imaging (MRI). We examined the feasibility of MRI-based detection of neuronal currents using computer simulations based on the laminar cortex model (LCM). Instead of simulating the activity of single neurons, we decomposed neuronal activity to action potentials (AP) and postsynaptic potentials (PSP). The geometries of dendrites and axons were generated dynamically to account for diverse neuronal morphologies. Magnetic fields associated with APs and PSPs were calculated during spontaneous and stimulated cortical activity, from which the neuronal current induced MRI signal was determined. We found that the MRI signal magnitude change (< 0.1 ppm) is below currently detectable levels but that the signal phase change is likely to be detectable. Furthermore, neuronal MRI signals are sensitive to temporal and spatial variations in neuronal activity but independent of the intensity of neuronal activation. Synchronized neuronal activity produces large phase changes (in the order of 0.1 milliradian). However, signal phase oscillates with neuronal activity. Consequently, MRI scans need to be synchronized with neuronal oscillations to maximize the likelihood of detecting signal phase changes due to neuronal currents. These findings inform the design of MRI experiments to detect neuronal currents.

Keywords: magnetic resonance imaging, neuronal current imaging, neuronal magnetic field

1 Introduction

A grand challenge facing brain research is to "see" neurons in action at high spatial and temporal resolution in the living human brain. Non-invasive techniques, notably electroencephalography (EEG), magnetoencephalography (MEG), and functional magnetic resonance imaging (fMRI), have provided invaluable knowledge about brain function in health and disease. However, EEG and MEG are low spatial resolution techniques for inferring neuronal activity from limited scalp measurements (Hamalainen et al., 1993; Niedermeyer and Lopes da Silva, 2005), and fMRI is a low temporal resolution method (Logothetis, 2008; Logothetis et al., 2001), which deduces brain activation indirectly from blood-oxygen-level-dependent (BOLD) changes driven by complex, non-linear hemodynamic processes (Huettel et al., 2009).

Neuronal activity produces small transient currents (Hille, 2001; Nunez and Srinivasan, 2006). These currents may be detectable using magnetic resonance imaging (MRI), because they produce small neuronal magnetic fields (NMF) which perturb the imaging magnetic field. As a result, changes in the precession frequencies of surrounding protons may modulate the MRI signal with information about neuronal activity (Bandettini et al., 2005; Hagberg et al., 2006; Kamei et al., 1999). Theoretically, this effect, termed neuronal current MRI (nc-MRI), has the potential to map neuronal activity with higher spatial and temporal resolution than existing neuroimaging methods (Bandettini et al., 2005). Successful implementation of nc-MRI would benefit the study of brain function and may also have important clinical applications, for example in the non-invasive mapping of epileptic foci (Liston et al., 2004). Previous MRI experiments attempting to capture neuronal current signal have been performed in a range of experimental preparations including turtles (Luo et al., 2009) and snail ganglia (Park et al., 2004) and in humans (Konn et al., 2004; Luo et

al., 2011b; Xiong et al., 2003) using various MRI sequences and a range of acquisition parameters. Results have been inconsistent even when similar MRI sequences and parameters have been used (for example, see Parkes et al., 2007; Xiong et al., 2003). Hence, the feasibility of nc-MRI is still debated (Bandettini et al., 2005; Hagberg et al., 2006).

Computer simulations are an important paradigm for predicting the nc-MRI techniques that are most likely to succeed. However, a major challenge for simulating the nc-MRI signal is to accurately model the spatial distribution and temporal variation of neuronal currents. Previous attempts have computed neuronal currents using an ensemble of identical neurons, for example an anatomically realistic pyramidal neuron from rat cortex (Blagoev et al., 2007), monkey hippocampus (Cassara et al., 2008), or human cortex (Luo et al., 2011a). This approach reduces the computational complexity inherent in simulating the dynamics of a large number of individual neurons. However, the MRI signal predicted by such models may be inaccurate for two reasons. First, morphological variations between neurons, which may have a significant impact on the size of calculated neuronal magnetic fields (NMF) (Cassara et al., 2008), are ignored. Second, models in which all neurons have identical firing patterns are likely to lead to unrealistic predicted time courses of neuronal current.

In the present work, we predicted the nc-MRI signal using the laminar cortex model (Du et al., 2012), a three-dimensional cortical network model incorporating realistic cortical architecture. We also simulated temporal variations in neuronal activity associated with realistic cortical architecture and neuronal morphology. The model was used to study the neuronal currents and predicted nc-MRI signal associated with different neuronal oscillatory states, at different levels of neuronal activity in the primary visual cortex of cats. The ability of current MRI techniques to detect predicted changes in MR signal magnitude and phase was also assessed.

2 Material and methods

2.1 Laminar cortex model (LCM)

We used the LCM (Du et al., 2012) to simulate neuronal activity of a grid of cortical columns. For a detailed description of the LCM the reader is referred to our previous work (Du et al., 2012), however we provide a general outline of the method here. The LCM treats the same type of neurons within a column as a group, which acts as a single entity in a network of neurons. The neuron groups have similar features to single neurons, but their dynamics and connections are averaged using the mean-field approximation (see Du et al., 2012; Wright, 2009). A synaptic connection map is used to control neuron group connections (Binzegger et al., 2004). Cortical laminar architecture is incorporated in the LCM, enabling simulation of neuronal activity in three-dimensions (see Figure 1A). The LCM was developed to simulate the neuronal activity of the visual cortex and validated under different conditions of visual stimulation.

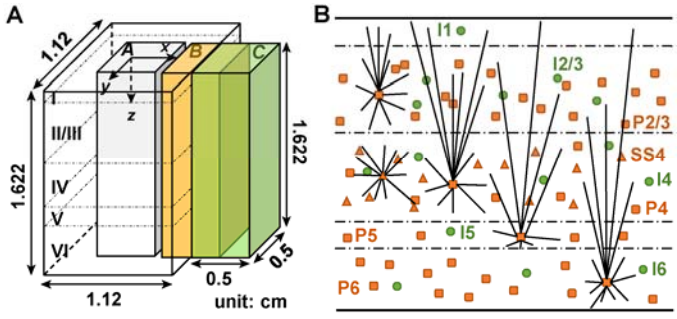

Figure 1 Structure of the model. The figure shows (A) the geometry of LCM simulated cortical region (transparent box) and three equal-size voxels (filled boxes), and (B) a sketch of cortical neurons and examples of dendrite tree structures.

We have now modified the LCM to incorporate additional features of cortical architecture. In the cortex, neurons may form synapses in multiple layers and the spatial distribution of synapses is essential for NMF calculation. Whereas the LCM originally did not consider the laminar

distribution of synapses and direct synaptic connections between neuron groups were assumed, the model now allows a neuron group to be connected to another neuron group via synapses in several layers. An example is given in Inline Supplementary Table S1 (Data were adopted from (Izhikevich and Edelman, 2008)). We also added a new spiny stellate (SS4) neuron group in layer IV, as these neurons have a different morphology and synaptic connection pattern to the pyramidal neurons of layer IV. The neuron groups of the new LCM are listed in Table 1.

Index	Neuron		Neurons under 1 mm² area	NMF calculated?
0	E1	Excitatory neuron in layer I	36	
1	I1	Inhibitory neuron in layer I	1177	
2	P2/3	Pyramidal neuron in layer II/III	20394	Yes
3	I2/3	Inhibitory neuron in layer II/III	5726	
4	P4	Pyramidal neuron in layer IV	7216	Yes
5	SS4	Spiny stellate neuron in layer IV	14433	Yes
6	I4	Inhibitory neuron in layer IV	5412	
7	P5	Pyramidal neuron in layer V	4785	Yes
8	I5	Inhibitory neuron in layer V	1098	
9	P6	Pyramidal neuron in layer VI	14198	Yes
10	I6	Inhibitory neuron in layer VI	3138	

Table 1 Neuron groups simulated in LCM. The neuron numbers were derived from (Beaulieu and Colonnier, 1983).

<Insert Inline Supplementary Table S1 here>

The LCM was used to simulate a cortical area of 1.12×1.12 mm², which is discretised to a 20×20 grid. The grid elements are of a size similar to mini-columns (about 56 micrometres) (Peters and Yilmaz, 1993). Simulation of a 60 second time course was performed starting at time t=0 seconds. After initialization, time evolution without particular stimulation for 50 seconds was simulated to allow the system to reach a steady state. Constant stimulation was commenced at time t=50 seconds (see Du et al., 2012 for details). The neuron membrane potentials of the last second were recorded and used for subsequent NMF calculations.

Spontaneous activity was simulated using the following parameter values: excitatory synaptic gain g_e = 0.9´ 10^{-6} V/spike, inhibitory synaptic gain g_i = 1.98´ 10^{-6} V/spike. Visual stimulation was simulated as white noise with mean=0 and deviation = 30 spike/sec (see Du et al., 2012 for details). Stimulated activity was produced using the following parameter values: g_e = 3.0´ 10^{-6} V/spike, g_i = 5.2´ 10^{-6} V/spike. The same visual stimulation was used. While multiple combinations of parameter values can result in similar neuronal activity, the parameter values provided above were empirically chosen to generate spontaneous and stimulated neuronal activity having different oscillation states (for details, see Du et al., 2012).

2.2 Axon and dendrite geometries

Neuronal membrane potentials generated by the LCM were used as the input for the NMF model. For each neuron, the number of APs at time t was given by:

$$N_q^{\mathrm{AP}}(t) = Q_q(V_q) \times \Delta t \qquad [1]$$

where $Q_q(x)$ is the spike generation function (see Du et al., 2012 for details), V_q is the neuron membrane potential of the group of neurons, and Δt is the time step, which was set to one millisecond. Each neuron was able to receive synaptic input from multiple presynaptic neuron groups. The number of PSPs was given by:

$$N_q^{\mathrm{PSP}}(t) = N_{qp}^{\mathrm{synp}} f_p(t) \times \Delta t \qquad [2]$$

where $f_p(t)$ is the efferent spike rate at the synapse determined by the firing state of the presynaptic neuron group, and N_{qp}^{synp} is the number of synapses from presynaptic neurons. We also assigned a

small random time delay ($< \Delta t$) to each AP and PSP to avoid unrealistic synchronizations between APs and PSPs.

The geometries of the axons and dendrites were generated dynamically. Axons and dendrites were modelled as straight cables between synapses and neuron bodies. Neuron bodies and synapses were evenly distributed within each cortical layer and each neuron was able to synapse with neurons in multiple cortical layers. The target synapse of an AP was randomly selected from all possible synapses for that neuron. For each neuron, we assumed that the target synapses for its APs within a given cortical layer were distributed according to a two-dimensional normal distribution (the standard deviation is set to 40 μm for I1, I2/3, SS4, I4, I5, I6 neurons, and 80 μm for E1, P2/3, P4, P5, P6 neurons) and that its afferent synapses were evenly distributed within a cylinder (the radius is set to 100 μm for all neurons) (see Figure 1B). The statistics of the APs and PSPs generated in the model are provided in Inline Supplementary Figure S1.

<Insert Inline Supplementary Figure S1 here>

To enable tractable simulations, we used a single membrane potential shape for all APs and for all PSPs separately (see

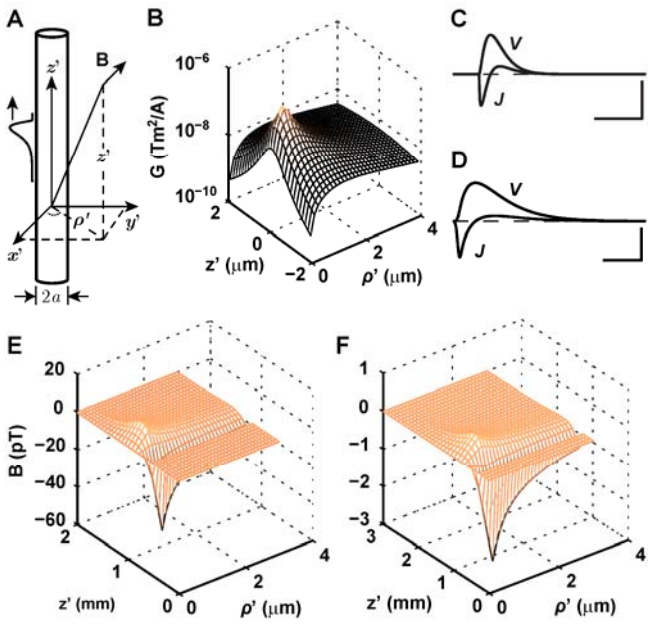

Figure 2), and their amplitudes were drawn from a Gaussian distribution (mean = 21 mV, standard deviation = 2.1 mV for APs, and mean = 1.2 mV, standard deviation = 0.12 mV for PSPs). We also assumed an exponential decay for PSPs with conduction along a cable (Johnston and Wu, 1995):

$$V^{PSP}(t,s) = \exp\left(-\frac{|s - s_0|}{l^{PSP}}\right) V^{PSP}\left(t - \frac{s - s_0}{v^{PSP}}, s_0\right) \quad [3]$$

where $V^{PSP}(t,s)$ is the membrane potential at position s at time t, s_0 is the synapse location on the dendrite, $v^{PSP} = 0.1$ m/sec is the velocity of PSPs, and $l^{PSP} = 333$ μm is the decay factor (Johnston and Wu, 1995). The conduction velocity of APs is $v^{AP} = 1.0$ m/sec and they were assumed not to change shape during propagation.

2.3 Magnetic field of APs and PSPs

Both APs and PSPs were modelled separately as membrane potential changes of biological cables. We calculated their magnetic fields using the method of Woosley et al. (Woosley et al., 1985). The magnetic field at a radial distance r from the cable was expressed as:

$$B(r,z) = G(r,z) \times J_z^-(z) = G(r,z) \times \left[J_z^i(z) - J_z^e(z)\right] \quad [4]$$

where Ä indicates convolution on z, a is cable radius (see

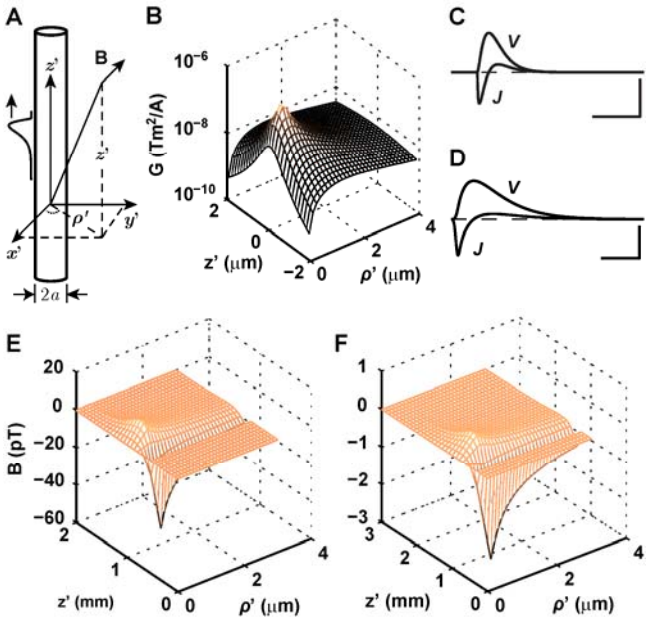

Figure 2), which was set to 0.5 μm for dendrites and 0.4 μm for axons, and J_z^i and J_z^e are the interior and exterior axial currents close to the cable membrane. In the Fourier domain, they are (Woosley et al., 1985):

$$\hat{J}_z^i(k) = -i\frac{\sigma^i g(k) k}{g(k)+1}\hat{V}(k), \qquad [5]$$

$$\hat{J}_z^e(k) = i\frac{\sigma^e k}{g(k)+1}\hat{V}(k), \qquad [6]$$

where k is the spatial frequency corresponding to the longitudinal coordinate z, $\hat{V}(k)$ is the Fourier transform of the membrane potential $V(z)$, and $g(k)$ are:

$$g(|k|a) = \frac{\sigma^e K_1(|k|a) I_0(|k|a)}{\sigma^i K_0(|k|a) I_1(|k|a)} .$$

where $I_0(x)$ and $I_1(x)$ are Bessel functions of the first kind and of first and second order, $K_0(x)$ and $K_1(x)$ are Bessel functions of the second kind and of first and second order, and $s^i = 1.0$ S/m and $s^e = 0.154$ S/m are interior and exterior media conductivities. The tilde denotes the Fourier domain. The Green's function $G(r,z)$, was formulated in terms of elliptic integrals:

$$G(r,z) = \frac{ma}{pB\sqrt{A+B}}\left\{A\mathbf{K}(m) - (A+B)\mathbf{E}(m)\right\}, \qquad [7]$$

where $m = 1.2566 \times 10^{-6}$ H/m is the permeability, $A = r^2 + a^2 + z^2$, $B = 2ar$, and $\mathbf{K}(m)$ and $\mathbf{E}(m)$ is the complete elliptic integrals of the first and second kind, respectively, and $m = 2B/(A+B)$ is the square of the elliptic modulus. A plot of the Green's function is provided in

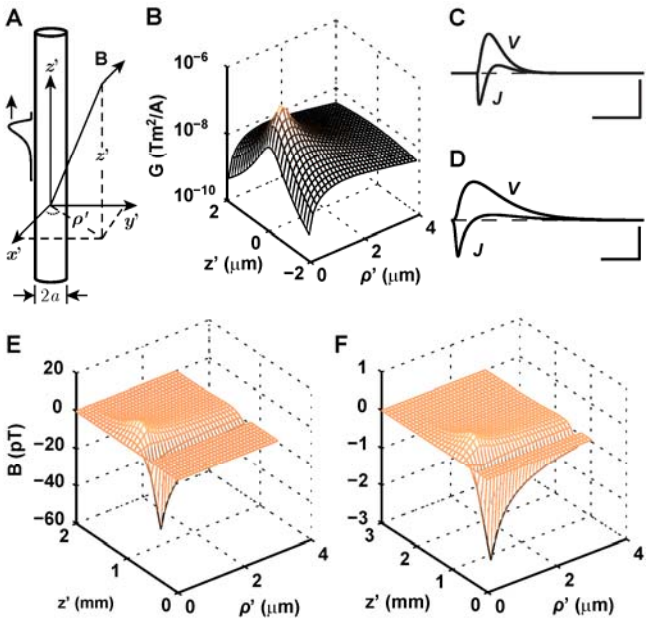

Figure 2.

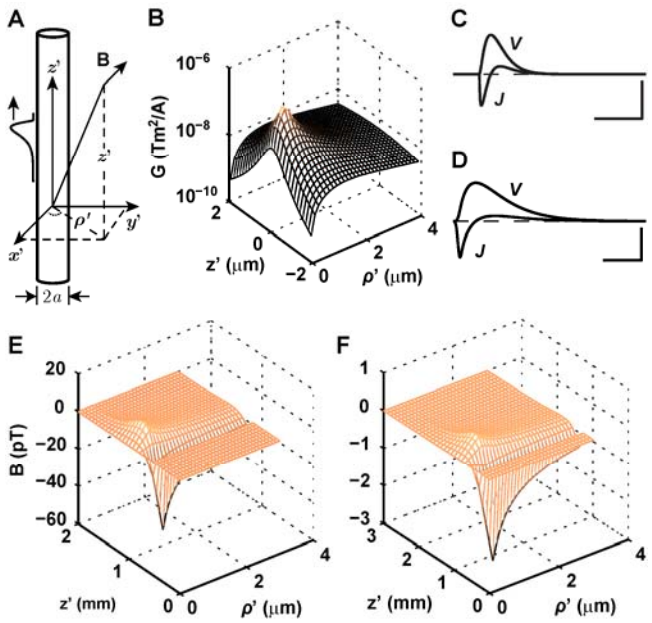

Figure 2 Magnetic fields of a single AP and a single PSP. Shown are (A) the coordinate system for AP and PSP magnetic field calculation, (B) a plot of the Green's function G (see Equation [7]), the shape (upper line) and surface currents (lower line) of (C) the AP (scale bar: 0.5 millimetre, 20 mV, 200A/m^2) and (D) the PSP (scale bar: 0.5 millimetre, 1.0 mV, 10A/m^2) used in the simulation, and the magnetic fields of the (E) AP and (F) the PSP. In (B), the Green's function G goes to zero when $\rho = 0$. See also Inline Supplementary Figure S1 for statistical information of the APs and PSPs for an animation of PSP magnetic fields.

2.4 Neuronal current MRI signal

The frequency of precession of protons is determined by the magnetic field present, which is a function of the scanner field (B_0) and the NMF. The NMF-induced phase changes accumulated during t_P (Heller et al., 2009):

$$j(\mathbf{r},t_0) = g\int_{t_0}^{t_0+t_P} B_n^{NMF}(\mathbf{r},t)\,\mathrm{d}t\ , \qquad [8]$$

where g = 2.675´ 10^8 rad/(T ×sec) is the proton gyromagnetic ratio, $B_n^{\mathrm{NMF}}(\mathbf{r},t)$ is the component of NMF aligned with B_0, t_p is the phase accumulating time (PAT), which is equivalent to the echo time

(TE) in gradient echo (GE) sequences, or the time to data acquisition (TA) in free induction decay (FID), and t_0 is the application time of radiofrequency (RF) pulse. If the proton density within a voxel is assumed to be homogeneously distributed, the MRI signal modified by neuronal currents is (Heller et al., 2009):

$$S = S_0 \frac{1}{V} \int_V \mathrm{d}^3 r \exp\left[-i\varphi(\mathbf{r},t) \right] \qquad [9]$$

where S_0 is the complex MRI signal without neuronal currents and V is voxel volume. The magnitude and phase change are:

$$\begin{aligned} \Delta s &= \frac{|S| - |S_0|}{|S_0|} = \frac{1}{V} \left| \int_V \mathrm{d}^3 r \exp\left[-i\varphi(\mathbf{r},t) \right] \right| - 1 \\ \Delta\varphi &= \arg\left\{ \int_V \mathrm{d}^3 r \exp\left[-i\varphi(\mathbf{r},t) \right] \right\} \end{aligned} \qquad [10]$$

where Δs and $\Delta\varphi$ are the fractional magnitude change and phase change of the nc-MRI signal. Since the magnitude of NMFs was much smaller than the magnitude of B_0, the small angle approximation for $\exp(-i\varphi)$ was applied:

$$\Delta s = \frac{1}{2}\left(\left\langle \varphi^2 \right\rangle - \left\langle \varphi \right\rangle^2 \right) + O(\varphi^4), \qquad [11]$$

$$\Delta\varphi = -\left\langle \varphi \right\rangle + O(\varphi^3), \qquad [12]$$

where $\left\langle \varphi \right\rangle$ and $\left\langle \varphi^2 \right\rangle$ denote the mean value of φ and φ^2 evaluated over the volume.

2.5 Simulation

The simulation program was written in the C++ programming language and compiled with the Intel® C++ Compiler version 2013.3.163 (x86_64, http://software.intel.com/intel-compilers/) on an

SGI® Altix® XE Cluster running SUSE Linux version 11 SP2 (x86_64, http://www.suse.com). The SGI® Message Passing Toolkit (http://www.sgi.com), a message passing interface implementation was used to parallelize the code to speed up program execution. The program was configured to run on 320 processors, and a run took around 48 hours to complete. The authors are willing to provide the source code upon request.

3 Results

We first examined the MRI signal induced by a single postsynaptic potential (PSP). We simulated a PSP propagating on a dendrite (see Figure 3). The magnetic fields of the PSP in two cubic volumes of interest (VOIs) were calculated. VOI 1 is symmetric about the dendrite, whilst VOI 2 is positioned alongside the dendrite. MRI signal magnitude and phase changes were calculated using different phase accumulating time (PAT). As shown in Figure 3, three interesting features of the signals in each VOI can be noted. First, the signal magnitude and phase changes in both VOIs tend to zero when phase accumulating time exceeds 20 milliseconds. Second, the phase change computed for VOI 1 but not VOI 2 is essentially zero. Third, the magnitude change for VOI 1 is at least three orders of magnitude larger than for VOI 2.

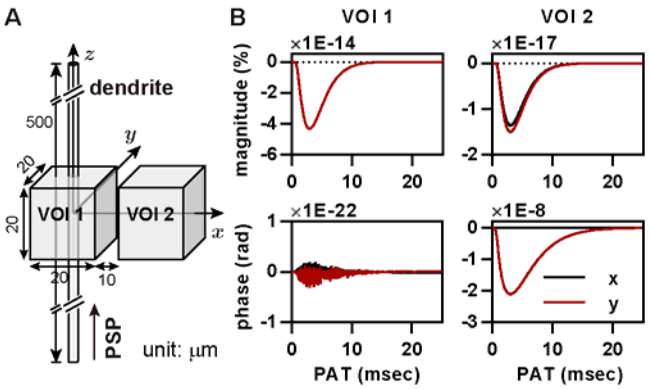

Figure 3 The MR signal changes induced by a single PSP. Shown are (A) a PSP on a straight dendrite and the two small volume-of-interest (named VOI 1 and VOI 2) in which the MR signal changes were calculated, and (B) the plot of the

phase and magnitude changes of the two VOIs as a function of phase accumulating time (PAT). The PAT starts at the same time as the PSP. The black and red lines in (B) show the signals produced by x- and y-component of NMFs, respectively. Notice the order differences of the signal changes.

To assess the influence of neuronal oscillation state on nc-MRI signals, two different oscillation states were generated using the LCM. Spontaneous activity corresponds to the activity in the primary visual cortex under natural visual stimulation and stimulated activity corresponds to activity induced by intermittent photic stimulation at a fixed frequency of 25 Hz. Average neuronal firing rates in the two states are plotted in

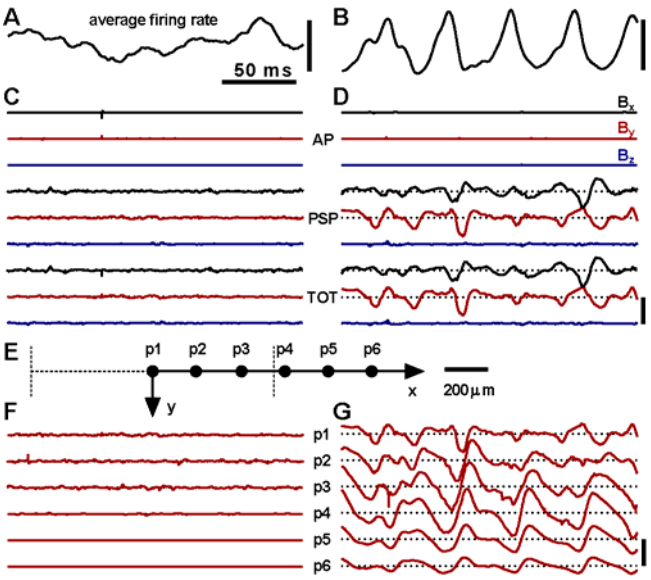

Figure 4. Spontaneous activity was characterized by a frequency spectrum of average firing rates dominated by low frequencies, while stimulated activity displayed an amplified oscillation around 25 Hz. The two states of neuronal activity were then used as inputs into the NMF model, and their effects on MRI signal phase and magnitude were calculated.

For numerical efficiency, we decomposed neuronal activities into action potentials (AP) and PSPs. The magnetic fields of APs and PSPs were calculated separately. Due to their different temporal scales, a time increment of one millisecond was used to simulate PSPs, and one tenth of a millisecond was used for APs. PSP magnetic fields were then linearly interpolated to correspond

with the time points set for APs. Total NMFs were obtained by summing AP and PSP magnetic fields, (see

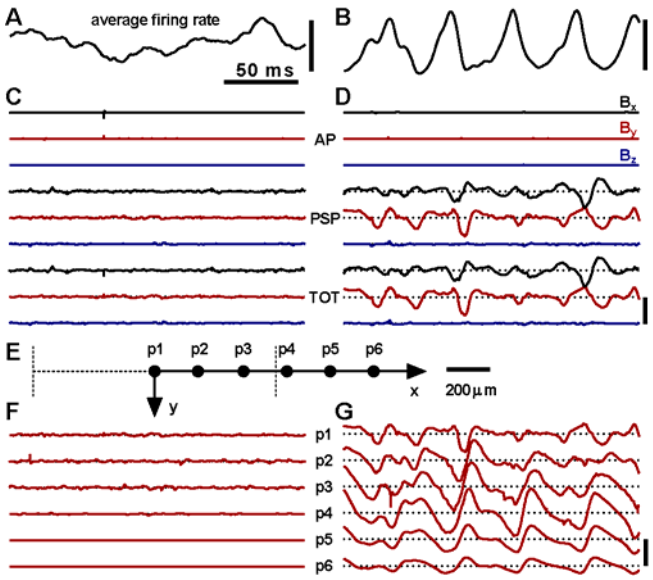

Figure 4 and Figure 5 for examples). As expected, the pattern of magnetic fields for APs differed significantly from that of PSPs. APs produce numerous sharp magnetic field peaks (small magnetic fields are not visible in

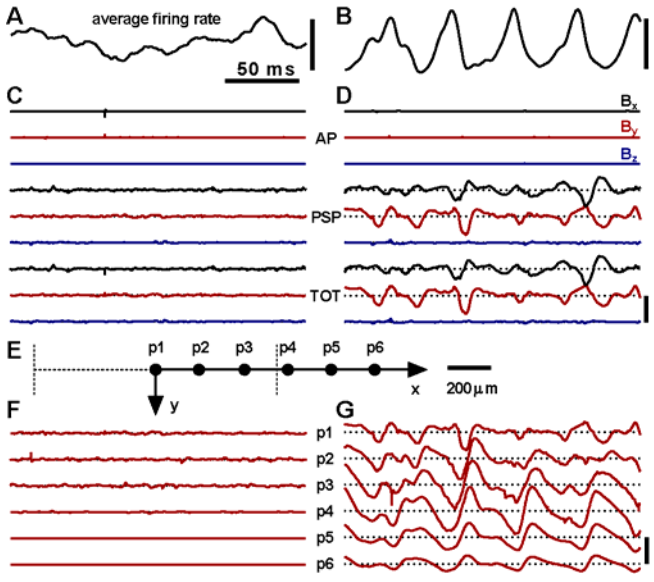

Figure 4 due to scaling), while PSPs produced smooth, comparatively slowly evolving magnetic fields. This difference can be explained by noting that a PSP lasts at least ten times longer than an AP. Stimulated activity produced NMFs about four times larger than spontaneous activity. Although neuronal firing rate was higher for stimulated activity, this is unlikely to be responsible

for the difference in NMFs. We noticed that large NMFs also arise with low firing rates during

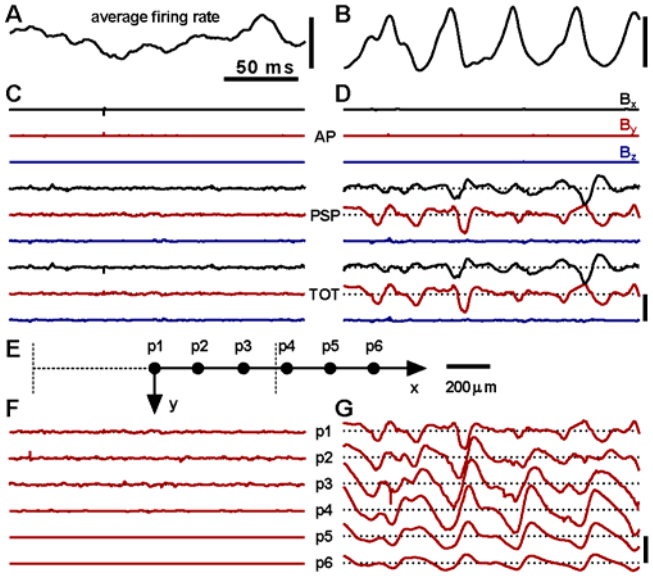

stimulated activity (see Figure 4 and Inline Supplementary Figure S2). This finding suggests that large NMFs are caused by oscillations in neuronal activity. Furthermore, NMFs during simulated spontaneous activity decayed rapidly outside the active region, to the extent that they dropped to almost zero at about 250 µm away from the region. NMFs with stimulated activity were larger outside than within the active region. Indeed, the largest NMFs with stimulated activity occurred just outside the active

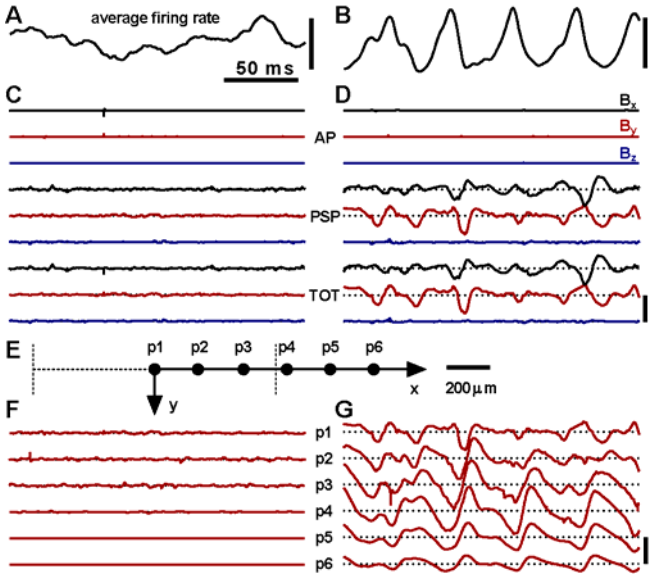

region (see

Figure 4, Figure 5 and Inline Supplementary Figure S2) and the NMFs decayed by about 50% at a distance of 500 μm. This finding suggests that collective flows of neuronal currents are produced during stimulated activity.

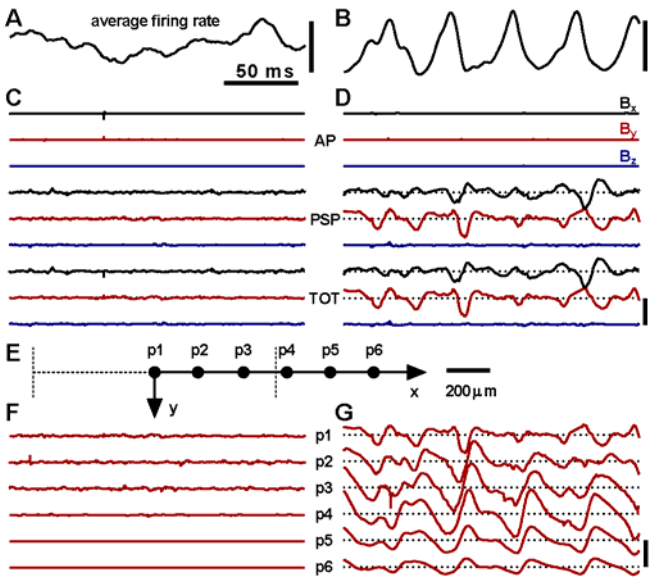

Figure 4 NMF time variations. Shown are the average neuronal firing rates of (A) spontaneous activity (scale bar: 0.001 spikes/sec) and (B) stimulated activity (scale bar: 20 spikes/sec), the AP, PSP and total NMFs at the centre of voxel A during (C) the spontaneous activity and (D) stimulated activity (scale bar: 500 pico-Teslas), and (E) the locations of six field points in the middle layer of the cortex and their NMFs during (F) spontaneous activity and (G) stimulated activity (scale bar: 500 pico-Teslas). The dotted baselines in (C-D) and (F-G) indicate zero magnetic field level. The black, red and blue lines in (C-D) depict the x-, y- and z-components of NMFs, respectively. The vertical dashed lines in (E) indicate the boundaries of the active region. In (F-G), only the y-components of the total NMFs are shown, see Inline Supplementary Figure S2 for x- and y-components.

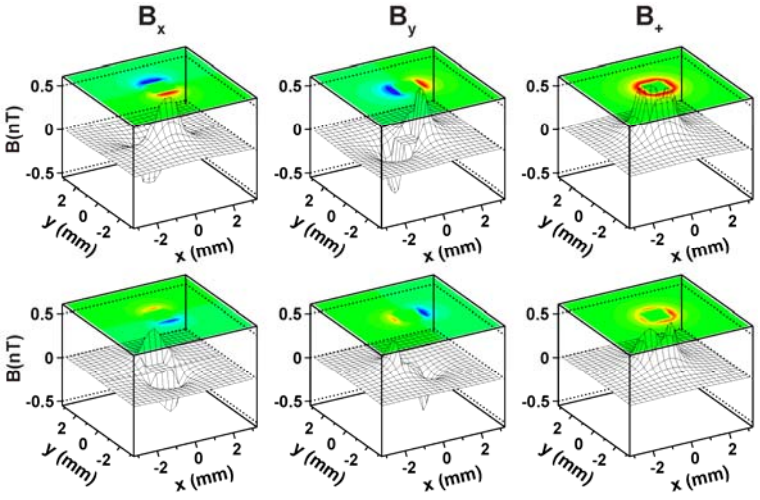

Figure 5 For the case of stimulated neuronal activity, illustrated are the spatial distributions of magnetic field components (B_x, B_y and $B_+ = \sqrt{B_x^2 + B_y^2}$) in the middle layer of the cortex at two different time points. Only magnetic fields outside the activated cortical region are shown.

<Insert Inline Supplementary Figure S2 here>

To validate our method for calculating the NMF, we simulated magnetoencephalography (MEG) signals induced by a short visual stimulus, and compared them with experimental measurements. We simulated MEG signals generated by a one centimetre square cortical region (see

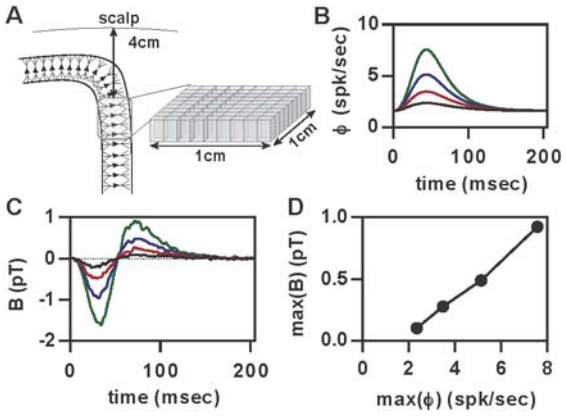

Figure 6). We divided the cortical region into a 9 × 9 grid, and used the LCM to simulate the neuronal activity of each element. Since the firing rates of neurons in a large cortical region have

been difficult to measure, the generated neuronal responses to stimulation were computed by multiplying the spontaneous activity neuronal membrane potentials by:

$$f(x) = \begin{cases} A l^{n} (t - t_0)^{n-1} \exp\left[l (t - t_0) \right] + 0.4 & t_0 < t < t_0 + t \\ 0.4 & \text{otherwise} \end{cases} \quad (13)$$

where t is the duration of the stimulus, $n = 3.2$, $l = 52$, and A was set to 0.01, 0.02, 0.03, 0.04 for four stimulation intensities. The use of the Gamma function accounts for the rapid increase of firing rates at the onset of stimuli and the slow decrease at the end of the stimuli, and these parameter values were chosen empirically to generate the average neuronal firing rates as shown in

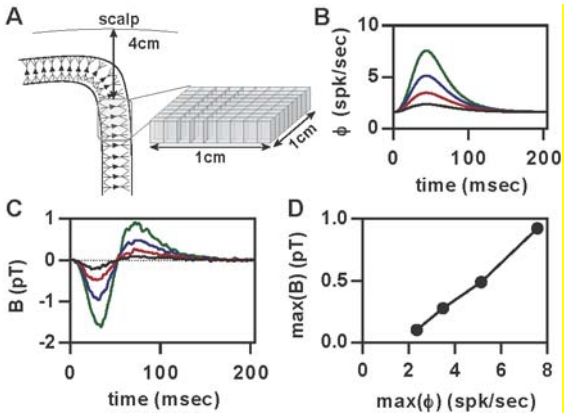

Figure 6B. The MEG signal was obtained by summing the magnetic fields of all elements and displayed two magnetic field peaks with opposite polarity, similar to the MEG signals observed in auditory cortex during brief exposure to an audible tone (Nakamura et al., 1997). The signal magnitude is of the same order of magnitude as the experimentally observed signal (Brenner et al., 1975). The linear relationship between the simulated intensity of neuronal activity and MEG signal magnitude was also comparable to the relationship between stimulation strength and measured MEG signal magnitude (Nakamura et al., 1997).

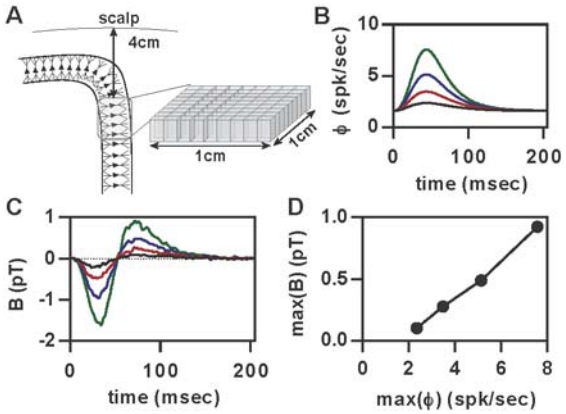

Figure 6 Simulated MEG signals. Shown are (A) the structure of the MEG model, (B) average neuronal firing rates used in simulation and (C) the corresponding simulated MEG signals, and (D) the relationship between neuronal firing rate intensity and MEG signal magnitudes.

To assess the spatial variation of nc-MRI signals, we calculated the neuronal current induced MRI signal magnitude and phase changes in three voxels: voxel A is located in the centre of the activated cortical region, voxel B is located on the boundary of the region (half the voxel is within the activated region and half is outside), and voxel C is located just outside the region (see Figure 1). In each of the voxels, neuronal magnetic fields were calculated at 3200 equally-spaced points and then used to evaluate nc-MRI signals. The results are shown in Figure 7 and Figure 8 (also see Inline Supplementary Figure S3). In general, we observed very small variations in signal magnitude, about 2-5 parts-per-billion (ppb) for spontaneous activity and 20-40 ppb for stimulated activity (phase accumulation time = 200 msec). A signal magnitude change of this size is well below the limit of detectability of current MRI techniques. However, larger relative changes in signal phase were observed, up to 15 μrad for spontaneous activity and 820 μrad for stimulated activity (phase accumulation time = 200 msec). Changes of this order of magnitude should be detectable using current MRI techniques. Moreover, changes in phase are larger at the boundary of the activated region. Phase changes in voxel B were larger than for voxels A and C for both spontaneous and stimulated activity.

The temporal evolution of the nc-MRI signal differed between spontaneous and stimulated activity. For spontaneous activity, signal phase in voxel A fluctuated about zero and signal magnitude increased over time suggesting that the magnetic fields within an active region are spatially inhomogeneous. In voxels B and C, changes in both signal phase and magnitude accumulated over time, suggesting that a homogeneous magnetic field component was the predominant influence. With stimulated activity, signal magnitude and phase evolution displayed recurring peaks at a frequency corresponding to neuronal firing rates (see

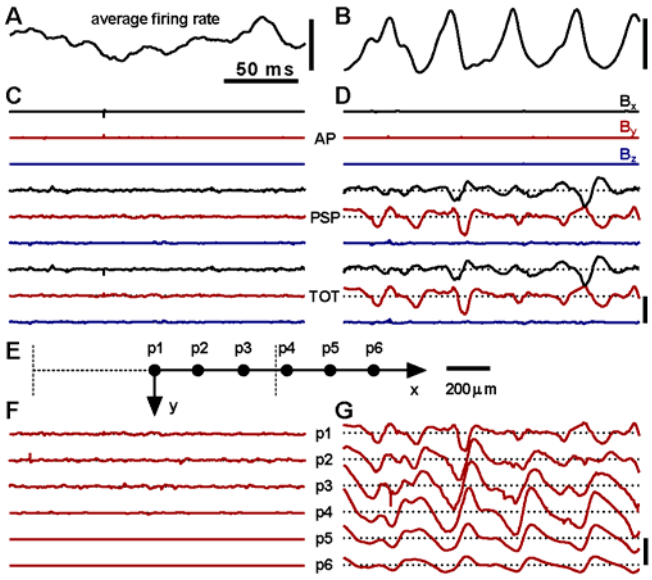

Figure 4). A relationship between firing rates and simulated signals was evident from our results

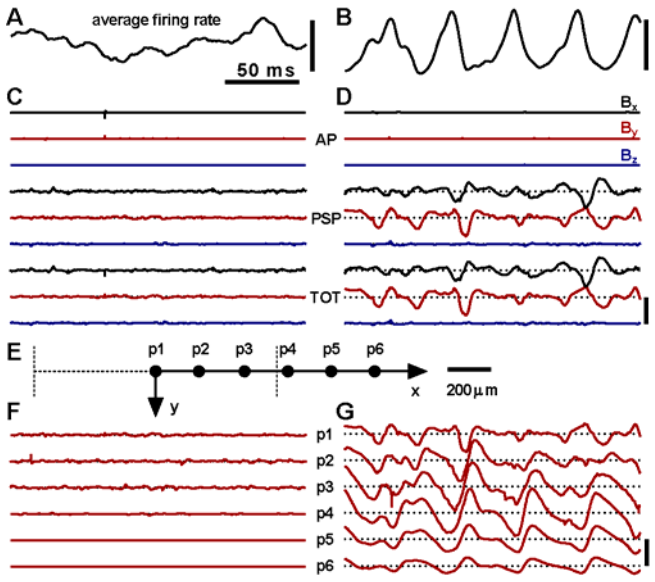

(see Figure 4 and Figure 7).

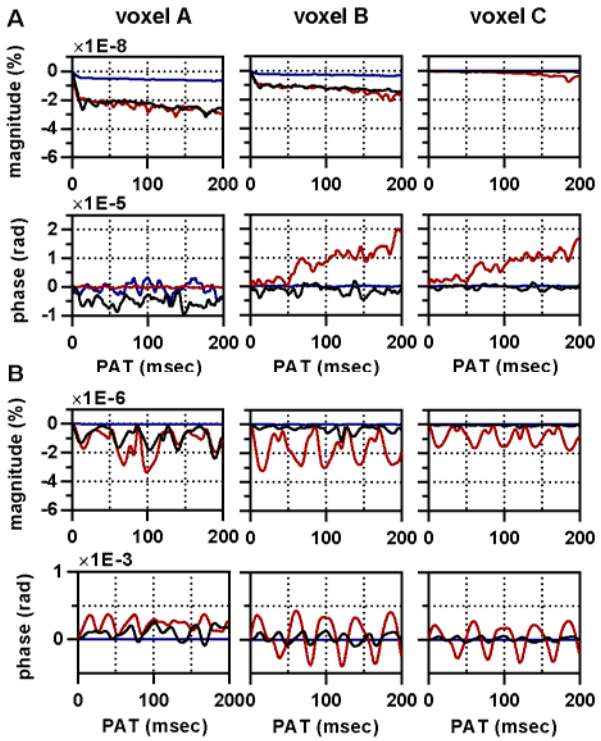

Figure 7 The MR signal magnitude and phase changes induced by spontaneous activity (A) and stimulated activity (B). *The signal changes are plotted against phase accumulating times. The black, red and blue lines show the signals produced by the x-, y- and z-components of NMFs, i.e. the signals predicted for the*

imaging fields (B_0) are aligned with x-, y-, and z-axes, respectively. Results were calculated from the same dataset as

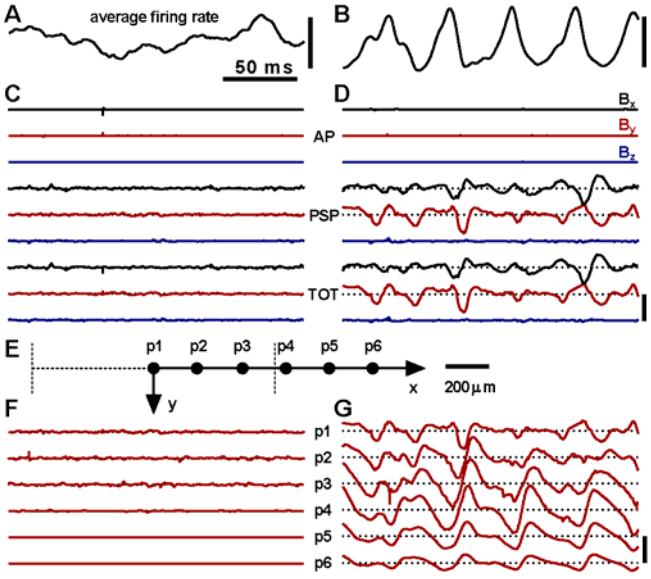

Figure 4. *See also* Figure 8.

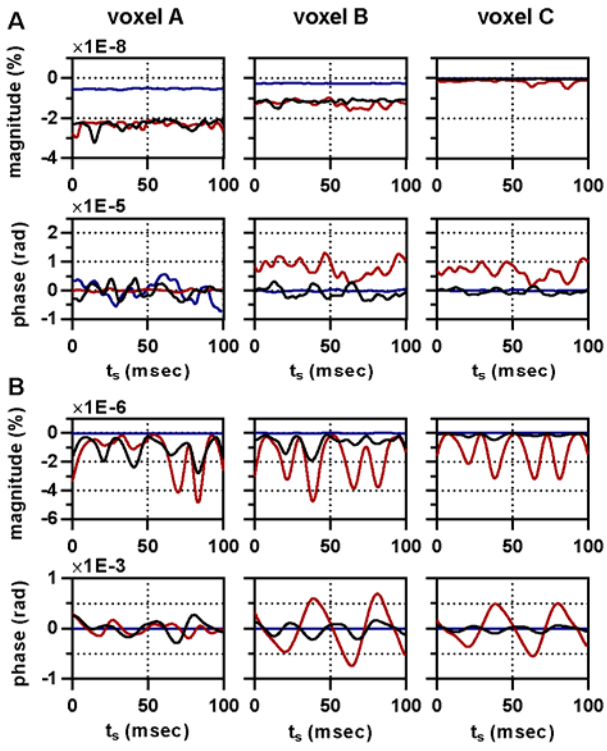

Figure 8 The dependence of nc-MRI signals on the starting point of phase accumulating time for spontaneous activity (A) and stimulated activity (B). *Shown are the nc-MRI signals calculated using phase accumulating times (PAT) starting at different times (t_s). The PAT was set to 100 msec. The black, red*

and blue lines show the signals produced by the x-, y- and z-components of NMFs, respectively. Results were calculated from the same dataset as

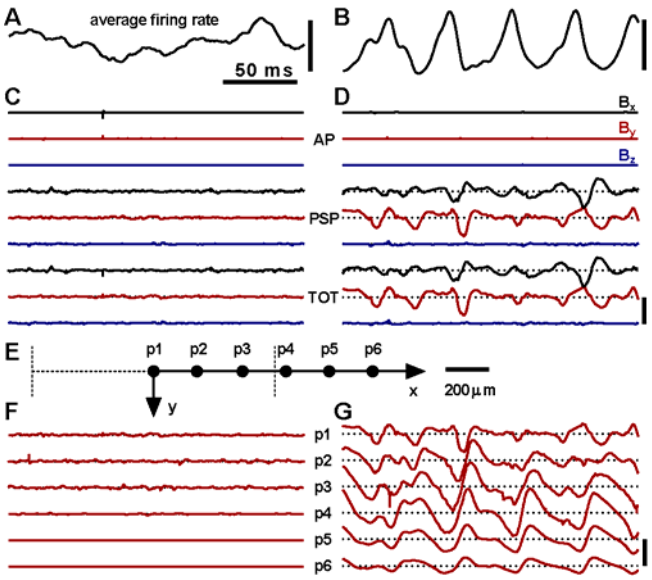

Figure 4. *The results shown in* Figure 7 *were calculated with* $t_s = 0$ *msec.*

<Insert Inline Supplementary Figure S3 here>

Due to the computational resources required by the simulations, we were not able to simulate directly the nc-MRI signal of large cortical regions and larger voxels. From the results shown above, however, we could estimate the MRI signal phase changes produced by a cortical region consisting of a number of sub-regions. We constructed an extended cortex region consisting of a matrix of 10x10 sub-regions (Figure 9A), each sub-region having the dimension and neuronal activity pattern as the cortical setup from above. We calculated the magnetic field components produced by each cortical region at sampling points inside and outside the extended region (see Figure 9A). To allow the magnetic fields produced by individual cortical sub-regions to be estimated, we assumed that the neuronal currents produced by the cortical sub-region are aligned with z-axis, and we adopted far field approximation of Biot-Savart's Law to assume that their magnetic field decay according to $1/r^2$ when away from the source. Then the magnetic field produced by a cortical sub-region at an

arbitrary location P outside the region can be expressed in terms of a known magnetic field of a reference point B as:

$$B_{Px} = \frac{r_B^2}{r_P^2}\left(B_{Bx}\cos q - B_{By}\sin q\right)$$
$$B_{Py} = \frac{r_B^2}{r_P^2}\left(B_{Bx}\sin q + B_{By}\cos q\right) \quad [14]$$

where r_B and r_P are the distance of the centre of the cortical sub-region to position P and B, respectively, and (B_{Bx}, B_{By}) is the magnetic field at point B. We used the centre of voxel B as the reference point, and assumed its magnetic fields is equal to the mean magnetic field of the voxel. When their magnetic fields inside the cortical sub-region cannot be estimated in a straightforward manner, because the far field approximation does not hold. We avoided this problem by placing the point in the centre of the sub-region and use the already calculated mean magnetic field of voxel A. The magnetic fields of five example sampling points highlighted in Figure 9A are provided in Table 2. We found the cortical region comprised of 100 sub-regions results in larger magnetic fields than a single cortical sub-region. At the boundary of the domain (the centre of voxel B and voxel II), for example, magnetic fields due to the extended cortical region were found to be 69.1% larger than those produced by the small cortical region of Figure 1.

We calculated the signal phase changes of three 4.5x4.5 mm voxels, labelled voxel I, II and III in Figure 9A. In each of the voxels, the magnetic fields produced by the extended cortical region are calculated at sampling 16 points and used to calculate the signal phase change. The results are shown in Figure 9C. In comparison to Figure 7, voxel I has the similar signal phase changes as voxel A, but voxel II has slightly larger signal phase changes than voxel B. Similarly, voxel III has slightly larger signal phase than voxel C. Overall, the increase in voxel volume from 2.0 mm^3 to 200

mm^3 has increased the signal phase change by approximately 17.6% at the edge and 11.2% away from the cortical region (peak to peak comparison for voxel B and II, and voxel C and III,), and the effect is negligible inside the cortical region (voxel I). To example the effect of voxel size on the phase signal, we have provided a extended cortical region result for voxel IV with dimensions 2.2x2.2 mm. We found a reduction in voxel volume leads to increased signal phase changes. Our results conclude that both voxel size and location affect NMF signals and experiments should be carefully planned to maximize the potential of observing an effect.

	B_x	B_y
P1	$B_{Ax} - 0.07B_{Bx} + 0.07B_{By}$	$B_{Ay} - 0.07B_{Bx} - 0.07B_{By}$
P2	$B_{Ax} + 0.07B_{Bx} - 0.07B_{By}$	$B_{Ay} + 0.07B_{Bx} + 0.07B_{By}$
P3	$1.22B_{Bx} + 0.04B_{By}$	$-0.04B_{Bx} - 1.22B_{By}$
P4	$0.39B_{Bx} + 0.02B_{By}$	$-0.02B_{Bx} + 0.39B_{By}$

Table 2 Expressions for the x- and y-components of the magnetic field for the four locations, as shown in Figure 9, as a function of the magnetic field of voxel A and B.

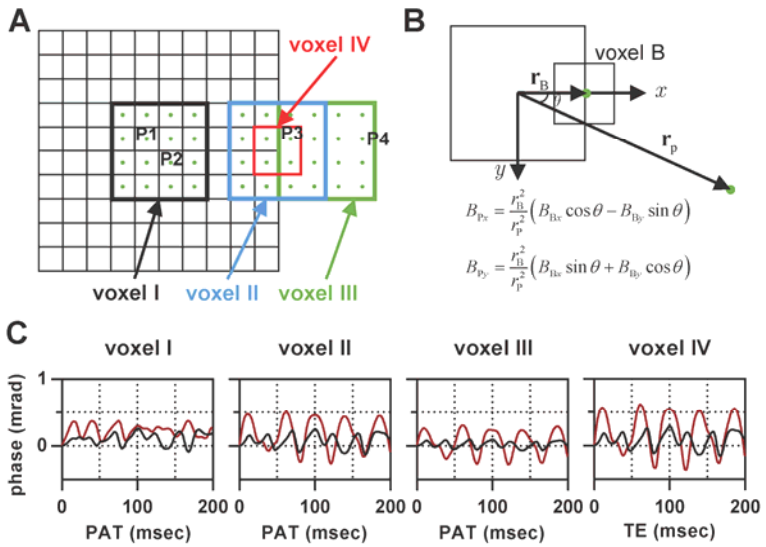

Figure 9 The MRI signal phase change produced by an extended cortical region consisting of 10x10 sub-regions. Shown are (A) the extended cortical region, the cortical sub-regions (gray squares), the locations of voxels of interest, and the sampling points, and (B) the analytic expression used to calculate the magnetic fields at location P, and (C) the MRI signal phase changes in four voxels in the

presence of a extended cortical region. The black and red lines in (C) show the signal phase produced by the x- and y- NMF components, respectively. The signal phases were calculated based on the same data as used in Figure 7.

4 Discussion

MRI-based detection of neuronal currents is yet to be convincingly demonstrated. An important technique to inform experimental design is to simulate realistic neuronal current distributions to study likely effects on MRI signal magnitude and phase. Here, we simulated the expected nc-MRI signal using a new NMF model based on our previous work. We have made three important advances over previous studies: a). the LCM was used to simulate neuronal activities with different types of neuronal oscillations, allowing their effects on the MRI signal to be elucidated; b). the LCM is based on a realistic cortical architecture incorporating lamination, cortical synaptic connections and varying neuronal morphology, all of which contribute to the simulation of realistic spatial neuronal current distributions; and c). we simulated the conduction of APs and PSPs, allowing the evolution of temporal NMF variations to be examined.

4.1 Neuronal current MRI signals

The signal differences between the spontaneous and stimulated activity and across the voxels predicted by our study may be explained by the temporal and spatial cancellation of NMFs.

Temporal cancellation occurs because PSPs comprise changes with opposing phases reflecting membrane depolarization and repolarization (see

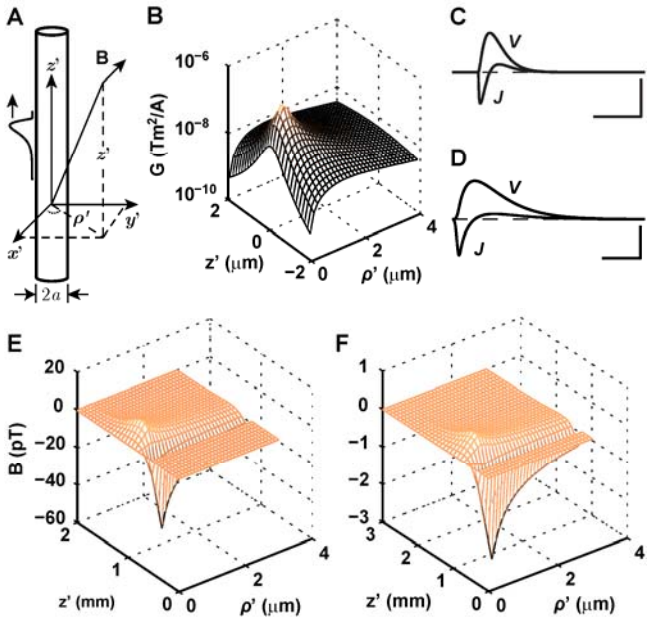

Figure 2). These produce sequential changes in magnetic fields of opposite sign with opposing effects on signal phase resulting in cancellation over time. Temporal cancellation may explain signal differences between spontaneous activity and stimulated activity. During spontaneous activity, neuronal activity is unsynchronized, with little correlation between PSPs. At any given time, there are almost the same number of membrane potential depolarizations and repolarizations taking place in a given volume. Because the produced magnetic fields largely cancel out, only the residuals contribute to the MRI signal. Temporal cancellation, however, diminishes during stimulated activity. Strong neuronal oscillatory behaviour produces synchronized PSPs, which exert their effects at about the same time. The PSPs also produce synchronized membrane potential depolarizations and repolarizations. The resulting collective membrane potential depolarization does not overlap with the collective membrane potential repolarization over time. Therefore, they do not cancel out but produce two sequential magnetic fields of opposite polarity. Synchronized neuronal activity thus produces oscillatory magnetic fields. Temporal cancellation does not affect AP magnetic fields because of their shorter durations.

Neuronal current MRI signals may also be damped by spatial cancellation of NMFs. In principle, a membrane potential change produces opposite magnetic fields on different sides of the axon/dendrite. If they are both included in a voxel, they may also cancel each other out, and contribute little to the mean NMF. The effect of spatial cancellation explains the differences observed between the three voxels studied. The MRI signal change for voxel A is strongly reduced through spatial cancellation, because the voxel is symmetric around the neuron. Voxels B and C have much weaker spatial cancellation, because they are located eccentrically with respect to the neuron. One consequence of spatial and temporal cancellation is that the nc-MRI signal does not depend directly on the intensity of neuronal activity. Instead, it is more likely to be a function of spatial and temporal differences (i.e. spatial gradients and temporal variations) in neuronal activity.

Our simulation results imply that the magnetic fields produced by PSPs are much larger than those produced by APs. The primary reason for this is that PSPs outnumber APs by a factor of thousands, and PSPs have a 10 times longer duration than APs. Our finding, however, does not agree with the result generated by the identical neuron model (Cassara et al., 2008), where APs were found to mostly contribute to the NMFs. Three factors may contribute to the discrepancy. Firstly, neurons of the identical neuron model were set to fire with the same temporal pattern. Therefore APs of all neurons completely overlapped and resulted in strong magnetic field peaks. Because the temporal pattern of APs in our model is asynchronous, strong NMF peaks due to firing of APs alone is unlikely. Secondly, the neuron in the identical neuron model has as little as 100 active synapses on the dendritic tree, while a neuron in our model can have more than 5000 synapses that are able to receive afferent spikes from other neurons. Consequently, in our model, neurons can have 50 or more times as many PSPs as those in the identical neuron model. Thirdly, back-propagation of APs

on dendrites is evident in the identical neuron model (see Figure 6 of (Cassara et al., 2008)) and is likely to add to the AP magnetic field peaks. Our model does not incorporate this effect.

We considered the effect of voxel size on signal phase change. Small voxels are likely to produce large phase changes. For example, the phase change of voxel IV (shown as a blue square in Figure 9) is 22% larger than that of voxel III. Furthermore, neuronal currents produce inhomogeneous magnetic fields that have peaks and troughs around the boundary of neuronal activity (see Figure 5). The averaging of NMFs within a voxel behaves as a low-pass filter with cut-off frequency determined by the inverse of the voxel size. Therefore, the magnetic field peaks and troughs can only be discerned by employing small voxels. The use of large voxels tends to reduce the magnetic field inhomogeneity and smooth out the peaks and troughs. In the extreme case when the voxel is much larger than the activated brain region, the signal phase change is zero, because magnetic fields must form closed loops (i.e. the curl of the magnetic field is zero).

Our simulation results indicate that neuronal current induced signal phase changes depend on the location of the voxel relative to the activated brain region, and a maximized phase change can be observed at the boundary of neuronal activity (see Figure 1 and Figure 9). Such a clear boundary of may not be present in the brain. Hence, cortical signalling is likely to be a combination of the behaviour observed for voxels A, B and C. Besides, the neuronal activity of a large brain region may not be synchronous, since oscillations of cortical sub-regions may have different phases. This spatial inhomogeneity of neuronal activity can reduce the level of spatial cancellation of NMFs, which may result in an increased neuronal current signal. The size of the effect depends on the extent of the spatial inhomogeneity of neuronal activity. Nevertheless, our simulations provide a platform to evaluate neuronal current signalling of the brain.

In a previous study, the neuronal current signals in organotypic rat brain cultures were measured (Petridou et al., 2006). A 3 to 14 mrad phase signal change and an absence of signal magnitude change at 3T with a spin-echo echo-planar imaging (TE = 60 msec, TR = 1sec) sequence were observed. The results confirm our prediction that neuronal current-induced signal phase changes are more pronounced than changes in signal magnitude. We compared the size of the observed phase change with our predictions. The volume of the culture (1.9-3.2 mm^3) is comparable to the cortical volume simulated in our model (2.0 mm^3, see Figure 1), but the volume of the voxel (24 mm^3) is about 60 times larger than the small voxels of Figure 1 (0.4 mm^3). Since the locations of the voxels relative to the culture are unclear, we have estimated the phase change in voxels with a similar volume at various locations. The maximum predicted signal phase change for voxels at different locations is in the range of 0.01-0.1 mrad. Therefore, the experimentally observed signal phase is around 140 times more than our prediction. Several factors may account for this difference. The seizure-like activity of the brain culture imaged in the experiments is likely to produce stronger neuronal currents than the neuronal activity generated by LCM. In our simulation, the amplitude of the neuronal oscillation is about 15 spikes/sec (from 10 spikes/sec to 25 spikes/sec), however, pyramidal neurons in the brain can fire at more than 100 spikes/sec. If a linear relationship between the oscillation amplitude and the signal phase change is adopted, the difference in neuronal activity may account for up to 10 times the difference. Furthermore, we assume a free induction decay or gradient echo sequence in our simulation, but a spin echo sequence was used in the experiments. The spin echo sequence may acquire two times larger signals, if the 180 degree refocusing pulse is applied when neuronal magnetic fields change sign (Petridou et al., 2006). Other factors, such as the shape of the culture and neuronal arrangement may also affect the predicted signal but their effects are difficult to estimate. Having taken all of these factors into consideration, the experimentally observed phase changes may still be 3-7 times bigger than we predict.

4.2 Implications for nc-MRI

Our simulation results imply that nc-MRI may not be useful as a general tool for imaging neuronal activity as a form of functional magnetic resonance imaging because nc-MRI signals are sensitive to spatial gradients and temporal variations as opposed to the intensity of neuronal activity. Given the small size of the signal, the results of this study predict that nc-MRI with current techniques may only be used to detect strong bursts of neuronal activity, as induced by stimuli or associated with pathological synchronised discharges such as epileptic seizures. Our simulations demonstrate that the magnitude change of the induced MRI signal change is too small to be detectable with current techniques but that the phase signal can potentially be detected. This coincides with previous experimental findings (Bodurka et al., 1999; Petridou et al., 2006). However, careful consideration must be given to experimental design.

A key prediction of our simulations is that synchronized neuronal activity produces a periodic phase signal (see Figure 7). In view of this, the echo times (TE) for MRI acquisitions should be matched with the frequency of neuronal activity to maximize the chance of observing an effect. Our simulation suggests that the optimal echo time is n+0.5 times the period of the major oscillation in neuronal activity, where n is a non-negative integer. For example, to measure a neuronal activity with 25 Hz oscillation (period = 40 msec), a time of 20, 60 or 100 msec should be chosen. Sample induction time needs to be appropriately chosen to ensure that NMFs do not change sign during the echo time. This requires MRI scans to be synchronized with the onset of stimulated neuronal activity.

It has been demonstrated that transient magnetic fields as small as 200 pico-Tesla lasting for 40 msec, similar to the NMFs predicted by our model, can be detected in phantoms using MRI (Bodurka and

Bandettini, 2002). But, detection of neuronal currents of the brain still faces numerous technical challenges. Neuronal activity is also associated with BOLD and diffusion signal effects, which may lead to temporal signal phase changes that mask the action of neurons. The BOLD effect produces signal phase changes that are approximately one tenth of a radian at 4 Tesla (Menon, 2002), which is two orders of magnitude larger than the neuronal current induced phase change. Water diffusion changes the phase of proton precession in a random manner. Essentially, the phase changes cancel and MRI signal magnitude decreases. Another challenge facing nc-MRI experiments is to suppress the noise caused by scanner instability and physiological processes, including respiration and cardiac actions. Scanner-related and physiological noise affect signal phase more prominently than signal magnitude (Hagberg et al., 2008; Petridou et al., 2009). Hagberg et al. (2012) showed the respiration-related signal phase change averaged across an imaging slice is about 280 mrad in the human brain at 3T, corresponding to a 0.012 ppm change of the imaging magnetic field, and the phase change due to the instrumentation and caused by thermal noise contribute at nearly the same level. They also demonstrated that high-pass spatial filtering can suppress the noise in signal phase to below 5 mrad, because the noise usually has a large spatial extent (> 1 cm) (Hagberg et al., 2012). In view of our simulation results, the noise in signal phase has to be further suppressed by at least one order of magnitude to be able to deduce the neuronal current induced signal phase change.

Our simulations also predict that the nc-MRI signal in the direction orthogonal to the cortex is likely to be significantly smaller than in the tangential (horizontal) direction, in line with the results of a previously conducted phantom (Bodurka et al., 1999) and simulation (Luo et al., 2011a) experiments. This is a natural consequence of the dendritic trees of pyramidal neurons being spread more widely in the vertical than in the horizontal direction. Because the architecture of cerebral cortical convolutions of the cerebral cortex results in multiple orientations of cortical neurons, nc-MRI needs

to be performed in at least two directions to capture the complete neuronal current signal (see, for exmaple, Lother et al., 2013), and images in all three coordinate directions are required to reconstruct the spatial distribution of signal sources.

In conclusion, we have developed a new model to calculate neuronal current induced MRI signal magnitude and phase changes. Our results suggest that the phase change produced by synchronized neuronal activity may be detectable with current MRI equipment whereas signal magnitude changes are below currently detectable levels. Signal acquisition timing and duration have to be appropriately chosen to maximise the effect of NMFs on the MRI signal.

5 References

Bandettini, P.A., Petridou, N., Bodurka, J., 2005. Direct detection of neuronal activity with MRI: Fantasy, possibility, or reality? Applied Magnetic Resonance 29, 65-88.

Beaulieu, C., Colonnier, M., 1983. The number of neurons in the different laminae of the binocular and monocular regions of area 17 in the cat, Canada. Journal of Comparative Neurology 217, 337-344.

Binzegger, T., Douglas, R.J., Martin, K.A., 2004. A quantitative map of the circuit of cat primary visual cortex. Journal of Neuroscience 24, 8441-8453.

Blagoev, K.B., Mihaila, B., Travis, B.J., Alexandrov, L.B., Bishop, A.R., Ranken, D., Posse, S., Gasparovic, C., Mayer, A., Aine, C.J., Ulbert, I., Morita, M., Muller, W., Connor, J., Halgren, E., 2007. Modelling the magnetic signature of neuronal tissue. NeuroImage 37, 137-148.

Bodurka, J., Bandettini, P.A., 2002. Toward direct mapping of neuronal activity: MRI detection of ultraweak, transient magnetic field changes. Magnetic Resonance in Medicine 47, 1052-1058.

Bodurka, J., Jesmanowicz, A., Hyde, J.S., Xu, H., Estkowski, L., Li, S.J., 1999. Current-induced magnetic resonance phase imaging. Journal of Magnetic Resonance 137, 265-271.

Brenner, D., Williamson, S.J., Kaufman, L., 1975. Visually evoked magnetic fields of the human brain. Science (New York, N.Y.) 190, 480-482.

Cassara, A.M., Hagberg, G.E., Bianciardi, M., Migliore, M., Maraviglia, B., 2008. Realistic simulations of neuronal activity: a contribution to the debate on direct detection of neuronal currents by MRI. NeuroImage 39, 87-106.

Du, J., Vegh, V., Reutens, D.C., 2012. The laminar cortex model: a new continuum cortex model incorporating laminar architecture. PLoS Computational Biology 8, e1002733.

Hagberg, G.E., Bianciardi, M., Brainovich, V., Cassara, A.M., Maraviglia, B., 2008. The effect of physiological noise in phase functional magnetic resonance imaging: from blood oxygen level-dependent effects to direct detection of neuronal currents. Magnetic Resonance Imaging 26, 1026-1040.

Hagberg, G.E., Bianciardi, M., Brainovich, V., Cassara, A.M., Maraviglia, B., 2012. Phase stability in fMRI time series: effect of noise regression, off-resonance correction and spatial filtering techniques. NeuroImage 59, 3748-3761.

Hagberg, G.E., Bianciardi, M., Maraviglia, B., 2006. Challenges for detection of neuronal currents by MRI. Magnetic Resonance Imaging 24, 483-493.

Hamalainen, M., Hari, R., Ilmoniemi, R.J., Knuutila, J., Lounasmaa, O.V., 1993. Magnetoencephalography - Theory, Instrumentation, and Applications to Noninvasive Studies of the Working Human Brain. Reviews of Modern Physics 65, 413-497.

Heller, L., Barrowes, B.E., George, J.S., 2009. Modeling direct effects of neural current on MRI. Human Brain Mapping 30, 1-12.

Hille, B., 2001. Ion channels of excitable membranes, 3rd ed. Sinauer, Sunderland, Massachusetts.

Huettel, S.A., Song, A.W., McCarthy, G., 2009. Functional magnetic resonance imaging. Sinauer Associates Inc.

Izhikevich, E.M., Edelman, G.M., 2008. Large-scale model of mammalian thalamocortical systems. Proceedings of the National Academy of Sciences of the United States of America 105, 3593-3598.

Johnston, D., Wu, S.M.-s., 1995. Foundations of cellular neurophysiology. MIT Press, Cambridge, Mass.

Kamei, H., Iramina, K., Yoshikawa, K., Ueno, S., 1999. Neuronal current distribution imaging using magnetic resonance. IEEE Transactions on Magnetics 35, 4109-4111.

Konn, D., Leach, S., Gowland, P., Bowtell, R., 2004. Initial attempts at directly detecting alpha wave activity in the brain using MRI. Magnetic Resonance Imaging 22, 1413-1427.

Liston, A.D., Salek-Haddadi, A., Kiebel, S.J., Hamandi, K., Turner, R., Lemieux, L., 2004. The MR detection of neuronal depolarization during 3-Hz spike-and-wave complexes in generalized epilepsy. Magnetic Resonance Imaging 22, 1441-1444.

Logothetis, N.K., 2008. What we can do and what we cannot do with fMRI. Nature 453, 869-878.

Logothetis, N.K., Pauls, J., Augath, M., Trinath, T., Oeltermann, A., 2001. Neurophysiological investigation of the basis of the fMRI signal. Nature 412, 150-157.

Lother, S., Hoelscher, U., Kampf, T., Jakob, P., Fidler, F., 2013. 3D gradient system for two B_0 field directions in earth's field MRI. MAGMA (Published ahead online 2013 Mar 23, DOI: 10.1007/s10334-013-0376-5), 565-573.

Luo, Q., Jiang, X., Chen, B., Zhu, Y., Gao, J.H., 2011a. Modeling neuronal current MRI signal with human neuron. Magnetic Resonance in Medicine 65, 1680-1689.

Luo, Q., Jiang, X., Gao, J.H., 2011b. Detection of neuronal current MRI in human without BOLD contamination. Magnetic Resonance in Medicine 66, 492-497.

Luo, Q., Lu, H., Lu, H., Senseman, D., Worsley, K., Yang, Y., Gao, J.H., 2009. Physiologically evoked neuronal current MRI in a bloodless turtle brain: detectable or not? NeuroImage 47, 1268-1276.

Menon, R.S., 2002. Postacquisition suppression of large-vessel BOLD signals in high-resolution fMRI. Magnetic Resonance in Medicine 47, 1-9.

Nakamura, A., Kakigi, R., Hoshiyama, M., Koyama, S., Kitamura, Y., Shimojo, M., 1997. Visual evoked cortical magnetic fields to pattern reversal stimulation. Brain research. Cognitive brain research 6, 9-22.

Niedermeyer, E., Lopes da Silva, F.H., 2005. Electroencephalography : basic principles, clinical applications, and related fields, 5th ed. Lippincott Williams & Wilkins, Philadelphia.

Nunez, P.L., Srinivasan, R., 2006. Electric fields of the brain : the neurophysics of EEG, 2nd ed. Oxford University Press, Oxford ; New York.

Park, T.S., Lee, S.Y., Park, J.H., Lee, S.Y., 2004. Effect of nerve cell currents on MRI images in snail ganglia. Neuroreport 15, 2783-2786.

Parkes, L.M., de Lange, F.P., Fries, P., Toni, I., Norris, D.G., 2007. Inability to directly detect magnetic field changes associated with neuronal activity. Magnetic Resonance in Medicine 57, 411-416.

Peters, A., Yilmaz, E., 1993. Neuronal organization in area 17 of cat visual cortex. Cerebral Cortex 3, 49-68.

Petridou, N., Plenz, D., Silva, A.C., Loew, M., Bodurka, J., Bandettini, P.A., 2006. Direct magnetic resonance detection of neuronal electrical activity. Proceedings of the National Academy of Sciences of the United States of America 103, 16015-16020.

Petridou, N., Schafer, A., Gowland, P., Bowtell, R., 2009. Phase vs. magnitude information in functional magnetic resonance imaging time series: toward understanding the noise. Magnetic Resonance Imaging 27, 1046-1057.

Woosley, J.K., Roth, B.J., Wikswo, J.P., 1985. The Magnetic-Field of a Single Axon - a Volume Conductor Model. Mathematical Biosciences 76, 1-36.

Wright, J.J., 2009. Generation and control of cortical gamma: findings from simulation at two scales. Neural Networks 22, 373-384.

Xiong, J., Fox, P.T., Gao, J.H., 2003. Directly mapping magnetic field effects of neuronal activity by magnetic resonance imaging. Human Brain Mapping 20, 41-49.

Figure Legends

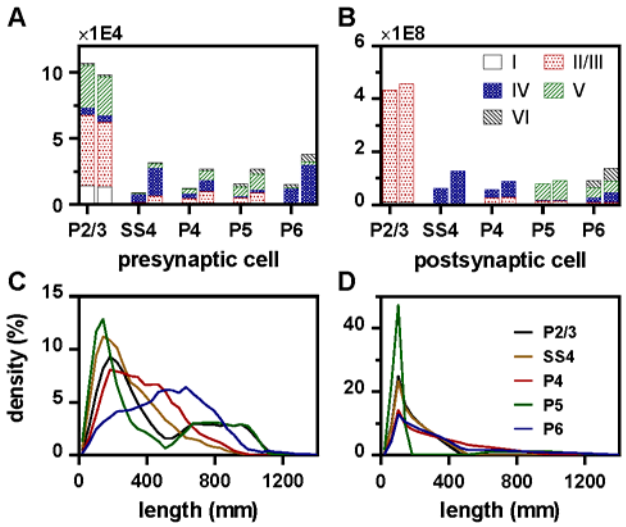

Figure S1 Statistics of the model. Shown are the numbers of (A) APs and (B) PSPs produced within 100 msec by spontaneous and stimulated activity, and the densities of (C) axon and (D) dendrite lengths. In (A-B), the left and right bars of each group show the results of the spontaneous and stimulated activity, respectively, and the bar patterns denote the target layers of APs in (A) and the location of PSP afferent synapses in (B).

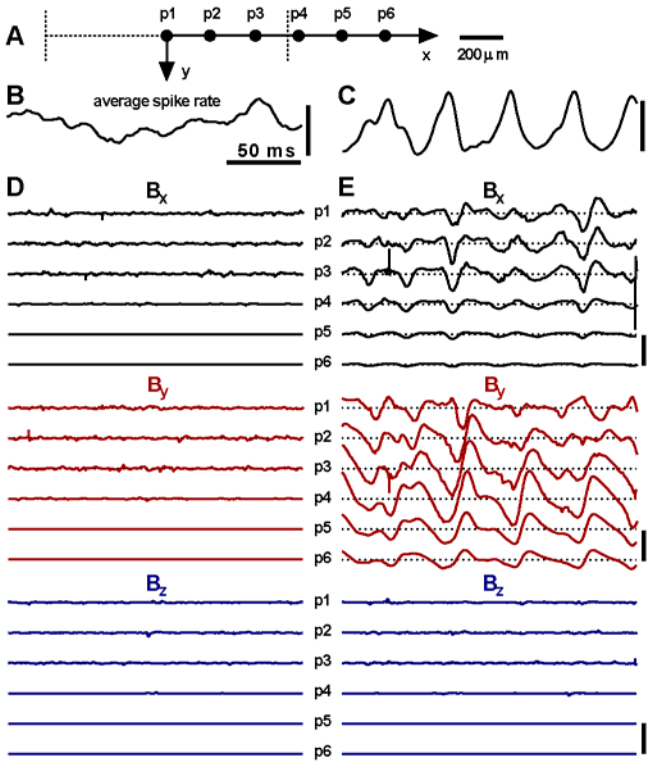

Figure S2 NMFs spatial variations. Illustrated are (A) the locations of six field points in the middle layer of the cortex for which NMFs are computed (the dashed lines denote the boundaries of the active region), (B) the average neuronal firing rates of the spontaneous activity (scale bar: 0.001 spike/sec) (C) and stimulated activity (scale bars: 20 spike/sec), and the NMFs during (D) spontaneous activity and (E) stimulated activity (scale bar: 500 pico-Teslas). Some of these results are also shown in Figure 2.

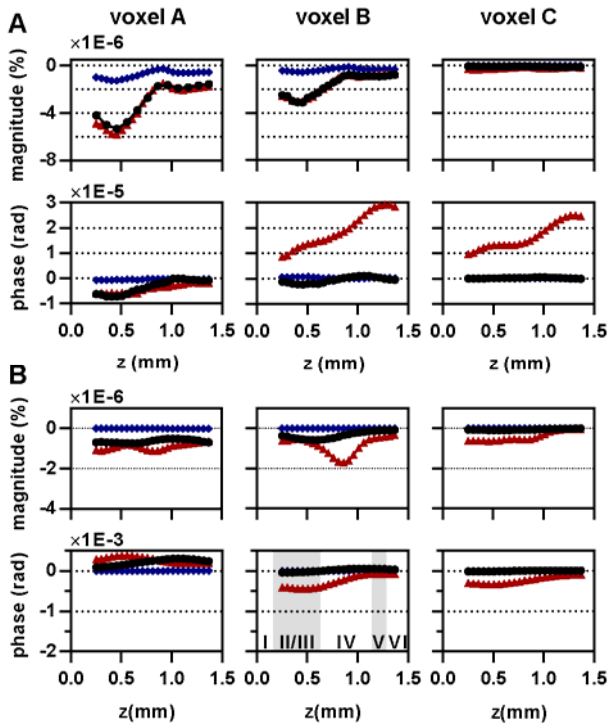

Figure S3 The nc-MRI signal magnitude and phase in different cortical depths. Shown are the nc-MRI signals in different cortical depths for (A) spontaneous activity and (B) stimulated activity (PAT=200msec). Each point represents a 1.12×1.12×0.5 millimetre voxel, and the z axis is located at voxel centre. Results were calculated from the same dataset as Figure 4. It should be pointed out that results shown here also vary with PAT window size and position.

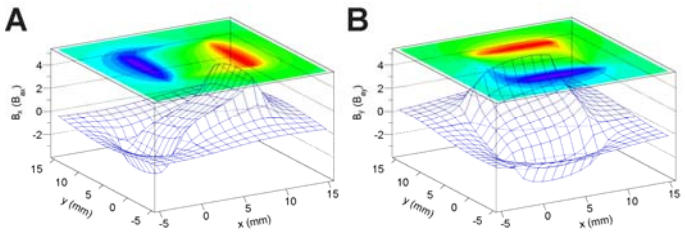

Figure S4 Spatial NMFs of an extended cortical region. The NMFs were calculated using the method shown in Figure 9. In the calculation, the following relationships were adopted, $B_{Ax} = B_{Ay} = B_{By}$ *and* $B_{Bx} = 4B_{By}$.

Table Legends

Presynaptic neuron	Postsynaptic neuron	Synapse location	Synapse number
P2/3	P5	layer I	85
		layer II/III	388
		layer IV	12
		layer V	2040
P5	P2/3	layer I	1
		layer II/III	429

Table S1 The synaptic connections between P2/3 and P5. Refer to Figure 9 in (Izhikevich and Edelman, 2008) for the complete cortical connection map.